# Epitaxial 2D PbS Nanoplates Arrays with Highly Efficient Infrared Response

*Yao Wen, Qisheng Wang, Lei Yin, Qi Liu, Feng Wang, Fengmei Wang, Zhenxing Wang, Kaili Liu, Kai Xu, Yun Huang, Tofik Ahmed Shifa, Chao Jiang,* Jie Xiong,* and Jun He**

2D materials such as graphene,[1] $MoS_2$,[2] $Bi_2Se_3$, and $Bi_2Te_3$[3] are now one of the most intensive studies owing to their unconventional surface-related physical, optical, and electronic properties. They are promising candidates in next-generation electronics and optoelectronics devices due to their fascinating properties including high electron or hole mobility,[1,4] quantum Hall effects,[5] superconductivity,[6] quantum anomalous Hall effect,[7] extraordinary thermal conduction,[8] and great potential applications in sensing,[9] transistors,[10] biomedicine,[11] photodetectors.[12] Benefiting from planar geometry, 2D nanostructures possess great advantages over the bulk materials for flexible devices and exhibit high compatibility with traditional microfabrication techniques. Furthermore, 2D nanostructures show surprising properties due to strong quantum confinement effect and ultrahigh specific surface area. However, the current research is mainly limited to the field of 2D layered materials such as graphene and $MoS_2$ as mentioned at the beginning. The exploration of 2D nonlayered materials will bring us exotic electronic and optoelectronic properties beyond layered materials due to novel electronic structure of nonlayered materials. As demonstrated in our previous work that 2D $Pb_{1-x}Sn_xSe$ nanoplates exhibit broad and sensitive infrared response due to its direct narrow bandgap and high absorption coefficient. Recently, Zhang et al. demonstrated the controlled epitaxial growth of 1D CdSe nanorods array on 2D CdS nanoplates. The nanorod arrays were grown on the selective facets of the hexagonal nanoplates via seed engineering. This hierarchical 1D/2D nonlayered nanostructures have great potential in a variety of fields such as energy conversion, electronics.[13] Xie et al. showed the ultrathin nanosheets of the Mn-doped $CoSe_2$ exhibited useful hydrogen evolution reaction properties, which provided a new way for newly highly efficient catalysts.[14] Therefore, the synthesis of 2D nonlayered materials is a pressing topic for their potential applications.

Precise control on the growth site of nanomaterial has been an essential and challenging topic. Significantly, individual crystal has shown great superiority in some applications, which require minimal cross-talk between neighboring devices including active matrix displays and sensor arrays.[15] Apparently, individual crystal arrays are critical in preparing practical devices with high performance and density. Throughout the history of van der Waals epitaxial 2D nanostructures arrays, it has achieved great progress but limited in layered nanostructures such as GaSe,[16] $Bi_2Se_3$, $Bi_2Te_3$, $In_2Se_3$, SnSe,[17,18] lead halide ($PbI_2$),[19,20] etc. Our group has made a big breakthrough in the growth and device applications of 2D nonlayered semiconductor such as van der Waals epitaxial 2D Te,[21] $Pb_{1-x}Sn_xSe$[22,23] nanoplates on mica or h-BN. However, patterning the 2D nonlayered semiconductor array is still a big challenge due to complicated growth dynamics of 2D nonlayered materials. Layered materials hold the intrinsic driving force for 2D anisotropic growth while 2D nonlayered materials lack this due to its 3D isotropic crystal structure. And crystal structure of layered materials matches well with layered epitaxial substrate (for example, $MoS_2$ shares the same hexagonal symmetry with growth substrate such as graphene, mica). However, nonlayered semiconductor exhibits completely different crystal orientation with layered epitaxial substrates.

Owing to the rapid deterioration of silicon photosensitive properties beyond 1100 nm, the narrow bandgap semiconductor has emerged such as $InAs_{1-x}Sb_x$, $Pb_{1-x}Sn_xTe$, $Hg_{1-x}Cd_xTe$, PbSe, PbTe, InAs, InSb, PbS.[24,25] These materials possess outstanding optoelectronics properties including high electron mobility, high optical absorption coefficient, and

Y. Wen, L. Yin, F. Wang, F. Wang, Prof. Z. Wang, K. Liu, K. Xu, Y. Huang, T. A. Shifa, Prof. C. Jiang, Prof. J. He
CAS Center for Excellence in Nanoscience
National Center for Nanoscience and Technology
Beijing 100190, China
E-mail: jiangch@nanoctr.cn; hej@nanoctr.cn

Y. Wen, Prof. C. Jiang
CAS Key Laboratory for Standardization and Measurement for Nanotechnology
National Center for Nanoscience and Technology
Beijing 100190, China

Y. Wen, L. Yin, F. Wang, F. Wang, Prof. Z. Wang, K. Liu, K. Xu, Y. Huang, T. A. Shifa
University of Chinese Academy of Sciences
Beijing 100049, China

Dr. Q. Wang
Department of Electrical and Computer Engineering
National University of Singapore
Singapore 117576, Singapore

L. Yin, F. Wang, F. Wang, Prof. Z. Wang, K. Liu, K. Xu, Y. Huang, T. A. Shifa, Prof. J. He
CAS Key Laboratory of Nanosystem and Hierarchical Fabrication
National Center for Nanoscience and Technology
Beijing 100190, China

Prof. Q. Liu
Key Laboratory of Microelectronic Devices and Integrated Technology
Institute of Microelectronics
Chinese Academy of Sciences
Beijing 100029, China

Prof. J. Xiong
State Key Laboratory of Electronic Thin Film and Integrated Devices
University of Electronic Science and Technology of China
Chengdu 610054, China
E-mail: jiexiong@uestc.edu.cn

**DOI: 10.1002/adma.201602481**

low thermal generation rate. As a typical example, $Hg_{1-x}Cd_xTe$ has shown great superiority in infrared (IR) radiation detectors owing to easy bandgap tailoring, multicolor detectors. However, $Hg_{1-x}Cd_xTe$ suffers nonuniformity over large area, surface instability, and complicated growth methods.[25] In contrast, PbS is easier to prepare and more stable with the direct narrow bandgap (0.4 eV).[26] Significantly, benefiting from the broad spectral detection from the visible to mid-IR region, PbS shows many applications in remote sensing and environmental monitoring,[27] biological imaging (transparent tissue windows from 800 to 1100 nm), telecommunications (1300 to 1600 nm), thermal imaging (1500 nm and beyond), thermal photovoltaics (>1900 nm).[28] Moreover, according theoretical predication, few-layer PbX (X = S, Se, Te) has an extremely high electron or hole carrier mobility.[29] Interestingly, a recent work displays the normalized carrier multiplication efficiency is higher in 2D PbS nanosheets compared with its 0D quantum dots, 1D nanorods, and 3D bulk state.[30]

Herein, we report epitaxial growth of ultrathin, highly efficient 2D nonlayered PbS nanoplates via van der Waals epitaxy. The nanoplates with thickness ranging from 5 to 35 nm was synthesized on graphite. The devices displayed outstanding photoresponsivity, detectivity, switching time and photogain values as high as 1621 A $W^{-1}$, $1.72 \times 10^{11}$ Jones, 0.3 s and 2512, respectively, which were even comparable with previously hybrid heterostructures.[31–35] Moreover, we achieved precise control over the orientation, position of PbS nanoplates on the flexible mica substrate. To the best of our knowledge, we for the first time realize the controllable synthesis of inorganic 2D nonlayered semiconductor arrays via van der Waals epitaxy, which is significant for exploring integrated infrared sensors.

**Figure 1**a shows schematic illustration of PbS crystal structure. Remarkably, unlike 2D layered nanostructures with strong planar covalent bonding in lateral dimension and weak van der Waals interaction between two adjacent layers, cubic-symmetry PbS is of 3D bonding with isotropic structure. The 2D PbS nanoplates were grown on layered mica and graphite. Figure 1b presents one of typical samples on graphite. The PbS powders were used as the precursor in a low-pressure chemical vapor deposition (LPCVD) systems. Interestingly, PbS nanoplates selectively grew on graphite, as shown in Figure 1b and Figure S1 (Supporting Information). The selective growth behavior could be explained by the classical nucleation kinetics as discussed in previous reports.[34,36] In our case, graphite without surface dangling bonds shows low surface energy ($\gamma_{graphite} \approx$ 70–80 mJ $m^{-2}$),[37] which is in favor of the lateral growth of PbS nanoplates along surface of graphite. In contrast, owing to the larger surface energy of $SiO_2$ ($\gamma_{SiO2} \approx$ 300–400 mJ $m^{-2}$),[34] the lateral growth of the PbS crystals on $SiO_2$/Si must be overcome large free energy barrier.[34] In addition, owing to the strong interaction between dangling bonds on the surface of 3D bonded $SiO_2$ and adatoms, the migration coefficient on $SiO_2$ is far lower than that on atomically smooth graphite surface.[22] Consequently, compared to $SiO_2$ surface, the lower surface energy and larger migration coefficient are the two key factors that PbS nanoplates selectively grew on graphite under optimized reaction parameters. Van der Waals epitaxy features weak van der Waals interaction between overlayer and substrate. It requires that either of overlayer or substrate is free of surface dangling bonds. Here we utilize mica and graphite as the growth substrate is based on the fact that they are both layered materials, the freshly exfoliated surfaces of which are highly smooth and chemically passivated. In addition, the van der Waals epitaxy allows a larger lattice mismatch between overlayer and substrate. That we see PbS nanoplates selectively grow on graphite but not $SiO_2$ substrates under the same

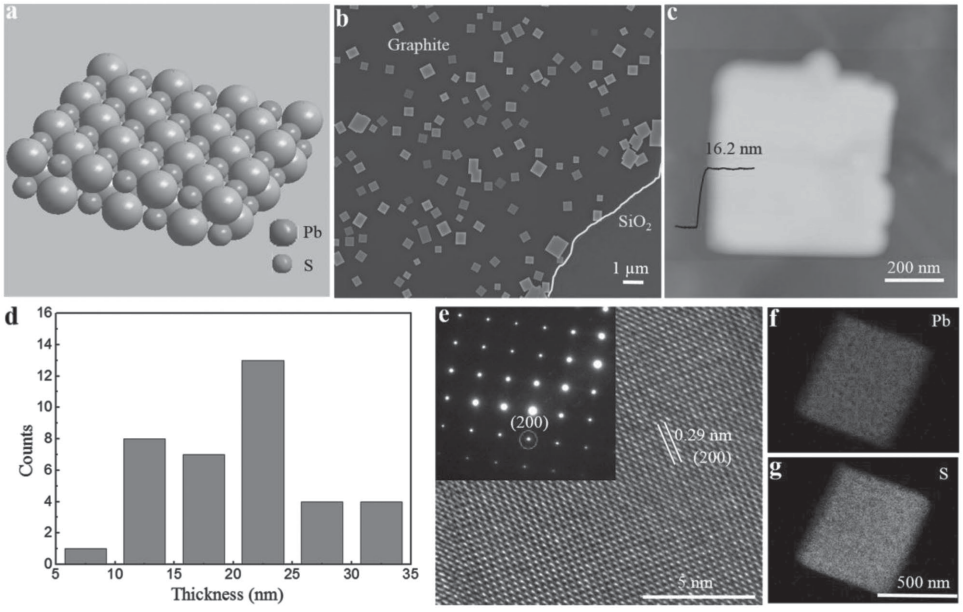


**Figure 1.** Morphology of vdWE PbS nanoplates. a) Schematic illustrations of the PbS with cubic crystal structure. b) SEM image of square PbS nanoplates on graphite. c) AFM image of one square nanoplate with thickness of 16.2 nm. d) The histogram statistics of nanoplates with thickness ranging from 5 to 35 nm. e) HRTEM image with clear crystal fringes of (200) planes with corresponding SAED as the inset. f,g) TEM–EDX mapping of PbS nanoplate.



Adv. Mater. 2016,
DOI: 10.1002/adma.201602481

growth conditions, which would be understood by the fact, as a conventional growth mode, large lattice mismatch between PbS (cubic) and $SiO_2$ (amorphous) hinders the epitaxy of PbS nanoplates on $SiO_2$. Figure 1c presents the atomic force microscopy (AFM) image of one square nanoplate with thickness of 16.2 nm. The thickness of PbS nanoplates is critical for the photoelectronic properties. The increase of nanoplates thickness will enhance the light harvesting. However, since photocurrent results from transport of photoexcited carriers, the signal-to-noise ratio likely decreases as the thickness of PbS nanoplates excesses the critical value. The numbers of photoexcited carriers are limited by the absorption coefficient. As the thickness of PbS nanoplates excesses the critical value, the underlayer of PbS nanoplate which has not been irradiated by laser will cause extra dark current. The thickness can be controlled by manipulating reaction time, carrier gas flow rate and temperature in the CVD process. The root-mean-square (RMS) roughness of nanoplates is less than 0.1 nm, which unambiguously verifies the atomically smooth surface of PbS nanoplate. The histogram statistics of thickness demonstrate that the thickness of nanoplates ranges from 5 to 35 nm, as shown in Figure 1d. The original AFM image presents in Figure S2 (Supporting Information). In order to investigate the crystallinity of the nanoplates, transmission electron microscopy (TEM) was employed. Figure 1e indicates the high-resolution TEM (HRTEM) images with clear crystal fringes of (200) planes, which demonstrates that the PbS nanoplate is well-defined single crystalline. The lattice constant of (200) planes is 0.29 nm. The top surfaces of the square nanoplate can be assigned to (002). As PbS possesses highly symmetry cubic structure, we can identify the edge orientation of PbS square nanoplates by direct TEM observation. As presented in inset of Figure 1e, the square SAED pattern reveals (200) planes of PbS nanoplates, indicating the edge oriented along [200] direction. The cubic crystal structure of PbS is confirmed by selected area electron diffraction (SAED), wherein the perfect cubic pattern clearly reveals the cubic symmetry and high crystallinity of the nanoplates. TEM–EDX elemental mapping (Figure 1f,g) indicates that Pb and S distribute uniformly in the entire nanoplate without detectable phase separation. An elemental quantitative analysis of TEM–EDX shows the atomic percentage ratio of Pb and S to be about 1:1.03, indicating ideal chemical stoichiometry.

The inset of **Figure 2**a shows the SEM images of the single PbS nanoplate device, which is transferred onto clean $SiO_2$/Si substrate from mica. The infrared photodetectors based on PbS nanoplates were fabricated on $SiO_2$/Si substrate by standard electron-beam lithography (EBL). Figure 2a presents the electrical transport characteristic of single PbS nanoplate. The obvious photoresponse can be detected with a series of wavelengths 800, 1064, 1340 nm lasers with effective intensity of 17.9, 15.1, 9.2 pW, respectively. The effective intensity means the laser power on the device channel. The effective irradiated area is about 0.69 $\mu m^2$. In addition, the linear plot of current ($I$)–voltage ($V$) curve exhibits the Ohmic contact in our device. Photoresponse of single PbS nanoplate at 800 nm laser is further executed, as shown in Figure 2b. The $I_{ph}$ ($I_{ph} = I_{illumination} - I_{dark}$) increases from 0.2 to 2.47 μA as the effective intensity varies from 0.6 to 60.4 pW, exhibiting the high detection sensitivity of our device. The photocurrent is linearly proportional to the incident light power $I_{ph} \approx P\beta$ with $\beta = 0.5$, as shown in Figure 2c.[38] The linear relationship indicates that the photocurrent is determined by photoconductive mechanism. The value of $\beta$ is expected to be 1 in ideal case. The recombination of the photogenerated free carriers and charge trapping

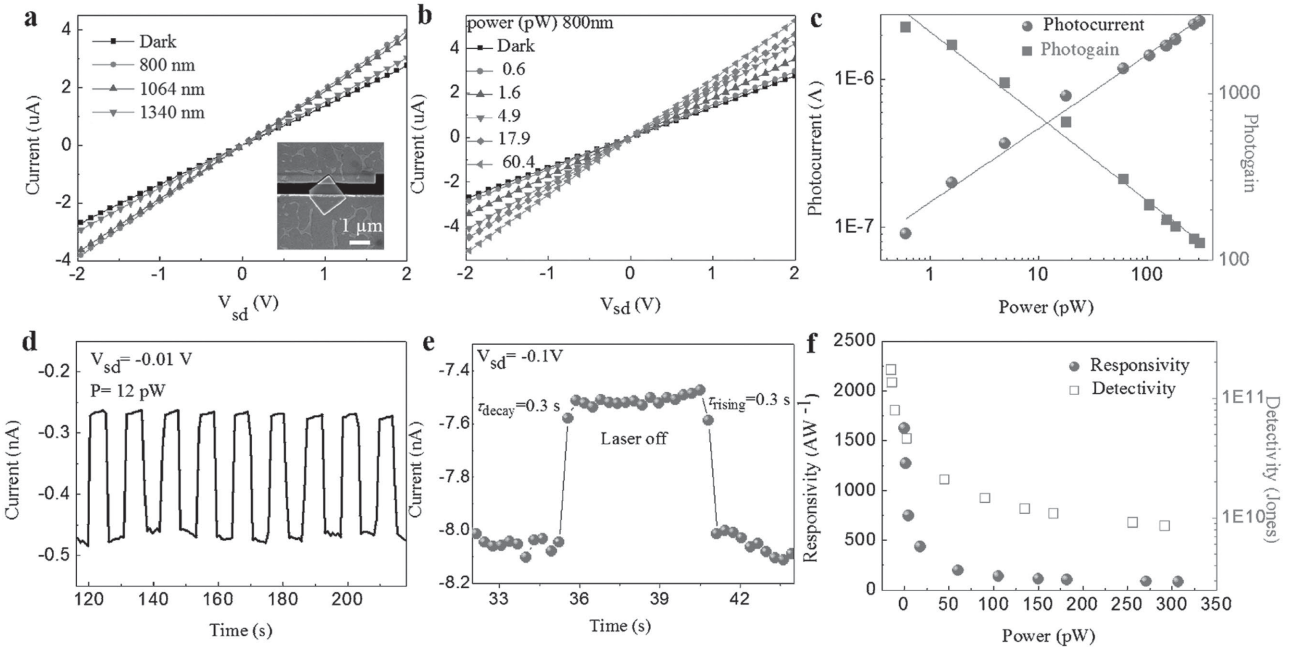


**Figure 2.** Infrared response of the PbS nanoplates device. a) Photoresponse of single PbS nanoplate with irradiation of 800, 1064, 1340 nm laser. b) Photoresponse of the nanoplate with irradiation of 800 nm laser. c) The plot of photogain (G) and photocurrent versus laser power at 800 nm. d) Time-dependent photoresponse of PbS nanoplate device at 800 nm. e) A separated response and reset cycle: $\tau_{rising} = \tau_{decay} = 0.3$ s, which corresponds to 100% rising and decay. f) The plots of responsivity and detectivity versus laser power.

**Table 1.** Comparison of optoelectronic parameters with hybrid heterostructures.

| | Wavelength | Responsivity | Response time[a)] | Refs. |
|---|---|---|---|---|
| PbS quantum dots-graphene | 600 nm | $5 \times 10^7$ [A W$^{-1}$] | $\tau_{rising} = \tau_{decay} = 2$ s | [31] |
| PbS quantum dots-graphene (CVD-grown) | 895 nm | $1 \times 10^7$ [A W$^{-1}$] | $\tau_{rising} = 0.3$ s<br>$\tau_{decay} = 1.7$ s | [32] |
| PbSe quantum dots-$MoS_2$ | >1200 nm | 1.9 [μA W$^{-1}$] | $\tau_{rising} = 0.25$ s<br>$\tau_{decay} = 0.43$ s | [35] |
| CdS nanoplates–$MoS_2$ | 610 nm | 3.91 [A W$^{-1}$] | $\tau_{rising} > 0.1$ s | [34] |
| PbS quantum dots-$MoS_2$ | 635 nm | $6 \times 10^5$ [A W$^{-1}$] | $\tau_{decay} = 0.35$ s | [33] |
| PbS nanoplates | 800 nm | 1621 [A W$^{-1}$] | $\tau_{rising} = \tau_{decay} = 0.3$ s | This work |

[a)] $\tau_{rising}$and $\tau_{decay}$ correspond to 100% rising and decay, respectively.

could be responsible for the loss of photocurrent.[38] In the ideal photoconductive detector, $I_{ph}$ is proportional to $P\beta$ with power factor $\beta$ of 1. In our case, $\beta$ equals to 0.5, indicating the loss of photogenerated electron-hole pairs. For example, the vacancies in PbS nanoplates form the localized states, which can trap the photoexcited carriers. And the unsaturated bonds on surface or interface of PbS nanoplates also behave as trap states centers, which capture photoexcited carriers. In addition, nonradiative recombination of electron–holes pair through phonon coupling is also responsible for loss of photo-excited carriers. Photogain ($G$) is given by the formula: $G = (I_{ph}/q)/(PS/h\nu) = h\nu R\lambda/q$, where $q$ is the electron charge, $h$ is Planck's constant, $\nu$ is the light frequency, and $R\lambda$ is responsivity.[39] The device exhibits great photogain as high as 2512, as shown in Figure 2c. Figure 2d exhibits time-resolved photoresponse at wavelength 800 nm with light power of 12 pW. The device is highly stable and reversible, which indicates almost the same level with light off. The magnified photoresponse cycle (Figure 2e) exhibits $\tau_{rising} = \tau_{decay} = 0.3$ s corresponding to 100% rising and decay, which is even comparable with previously hybrid heterostructures, as shown in **Table 1**.[31–33,35] The responsivity ($R$) is defined by $I_{ph}$/PA, $A$ is the irradiated area, $P$ is the light density. We extract the responsivity ($R$), which maintains in the range of 81 to 1621 A W$^{-1}$ as effective intensity distributing between 306.7 and 0.6 pW as shown in Figure 2f. The responsivity represents the ability of light harvesting. Significantly, when effective intensity drops to 0.6 pW, $R$ dramatically increases to 1621 A W$^{-1}$ which is even better than previously hybrid heterostructures,[34,35] as shown in Table 1. Detectivity ($D^*$) can be expressed as $D^* = I_{ph}A^{1/2}/PA(2qI_{dark})^{1/2}$. In our case, $D^*$ values of ≈1.72 × $10^{11}$ Jones is achieved at $P = 0.6$ pW, as shown in Figure 2f.

Significantly, the practical infrared detectors require minimal cross-talk between neighboring devices.[15] Therefore, individual crystal has shown great superiority than thin film. Here, we precisely controlled the orientation, position of the cubic PbS nanoplates on the flexible fluorophlogopite [$KMg_3(AlSi_3O_{10})F_2$] mica substrate. Mica with a pseudohexagonal $Z_2O_5$ (Z = Si, Al) layered structure is an ideal chemically inert and atomically planar surface for vdWE. Orientation-controlled growth of PbS nanoplates is crucial for next-generation integrated optoelectronic circuits. **Figure 3**a exhibits optical microscope (OM) images with orientation-controlled 18 × 16 arrays of square PbS nanoplates on mica. The

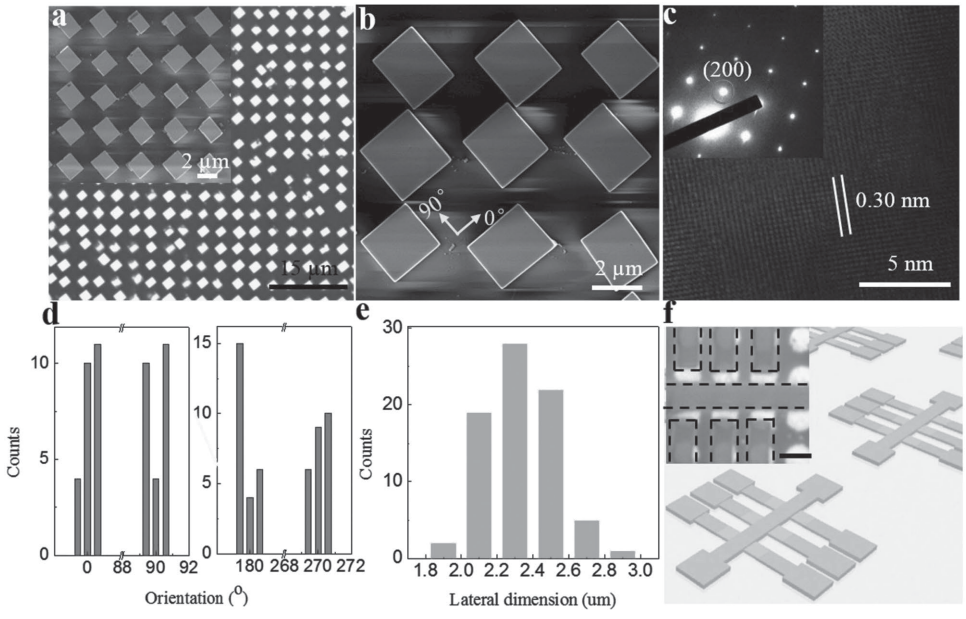


**Figure 3.** Morphology of 2D PbS nanoplates arrays. a) OM image of orientation-controlled 18 × 16 PbS nanoplates arrays on mica. The inset shows SEM image of 5 × 5 PbS arrays. b) Magnified SEM image of 3 × 3 PbS arrays. c) HRTEM image of the single PbS with corresponding SAED as the inset. d) Histogram of the orientation distribution of PbS arrays obtained from 50 nanoplates. The edges of square nanoplates on mica are oriented predominantly at multiples of 90°. e) Histogram of the lateral dimension of PbS arrays obtained from 77 nanoplates. f) Schematic illustration of PbS integrated device arrays, top insert: OM image of PbS-integrated device arrays, the scale bar is 2 μm.



*Adv. Mater.* **2016**,
DOI: 10.1002/adma.201602481

well-ordered 5×5 and 3×3 arrays of square PbS are also presented in the SEM images (the inset of Figure 3a,b). HRTEM and corresponding SAED images of the individual PbS nanoplate reveal that nanoplates are well-defined single-crystalline phase with clear crystal fringes of (200) planes, as shown in Figure 3c. We have executed the XRD on PbS nanoplates arrays. As shown in Figure S7a (Supporting Information), the peaks of (111), (200), (220), (222), (400) are consistent with standard JCPDS card (PDF#77-0244), indicating the highly single-crystalline of PbS nanoplates. We have performed the UV–VIS–NIR spectroscopy on PbS nanoplates arrays. As we can see from Figure S7b in the Supporting Information, it exhibits a broad absorption from 200 to 840 nm, which matches well with its narrow bandgap (0.4 eV). The cutoff of spectra absorption (theoretically 3100 nm) has not been observed due to limited detection range (200–840 nm) of our UV–vis–infrared spectroscopy. From the absorption spectra, we can see 800 nm lasers are suitable for photoresponse measurements. To quantitatively describe the orientation-controlled PbS nanoplates, well-ordered arrays with 50 nanoplates are analyzed as shown in Figure 3d. The edges of square nanoplates on mica are oriented predominantly at multiples of 90°. Compared with the random orientation of the PbS nanoplates grown on graphite, the orientation-controlled growth of nanoplates indicates that the epitaxial nature between mica and PbS is crucial for well-ordered arrays.[3,16–18,34,40,41] Although the mechanism merits further investigation, we propose one possibility to elucidate the epitaxial relation between PbS nanoplates and mica. The lattice constant of mica corresponds to $a$ = 0.53 nm, $b$ = 0.92 nm, and $c$ = 1.01 nm.[40] Noticeably, the surfaces of mica (00n) are predominantly occupied by K atoms, as previously reported.[40] As shown in Figure S3 (Supporting Information), the hexagonal K atom pattern of mica (00n) surfaces brings about four equivalent epitaxial relations with PbS final exposed four {200} crystal surfaces, which results in four orientations (0°, 90°, 180°, and 270°) of PbS nanoplates arrays. The lattice mismatch between {100} lattice planes (0.59 nm) of PbS (JCPDS card NO. 78-1897) and the K atoms (0.53 nm) is 11%. Owing to the weak van der Waals interaction at the interface, van der Waals epitaxial allows large lattice mismatch, such as 32% for CdS and $MoS_2$, 12% for PbSe and $MoS_2$, 6% for $Pb_{1-x}Sn_xTe$ and mica.[34,35,40] The ordered growth of PbS nanoplates array further confirms the nature of van der Waals epitaxy as PbS shows a lattice mismatch with mica as large as 11%. A high-quality interface between PbS nanoplates and substrate is expected although the interface lattice orientation has not been directly observed due to the difficulties in fabricating the cross-sectional sample. In the van der Waals epitaxy, the weak interaction in the interface allows strain relaxation, which is less possible in conventional epitaxial growth. Statistics of SEM images give the lateral dimension distribution ranging from 1.8 to 3 μm, which exhibits the highly controlled lateral sizes of nanoplates, as shown in Figure 3e. Figure S4 (Supporting Information) exhibits the AFM image and height profile (white dashed line) of PbS nanoplates, which shows flat surfaces with thickness ranging from 100 to 200 nm. Figure 3f exhibits the schematic illustration of PbS-integrated device arrays. The inset shows the 3×2 device arrays on mica.

We realize epitaxial PbS nanopliates array by utilizing NaCl aqueous solution to define the selectively van der Waals epitaxy of PbS nanoplates. First, mica was intaglioed by NaCl aqueous solution using a polydimethylsiloxane (PDMS) stamp,[18] as shown in **Figure 4**a. Then, mica with NaCl aqueous solution were heated to 150 °C using a heating belt. Finally, the mica surface modified with periodic arrays was released from the PDMS stamp. Benefiting from the hydrophilic surface of mica, uniform patterns can be achieved, as shown in Figure S5 (Supporting Information). After printing and drying, selective-area van der Waals epitaxy of PbS crystals was employed.[41] In order to reveal the growing mechanism of PbS nanoplates arrays, the surface morphology of the PbS nanoplates was investigated by SEM under different reaction times. Interesting, a large amount of small white dots distributes evenly in the entire growth substrate with the reaction time of 30 s, regardless of exposed periodic mica arrays and modified NaCl surface as shown in Figure 4b. Increasing reaction time to

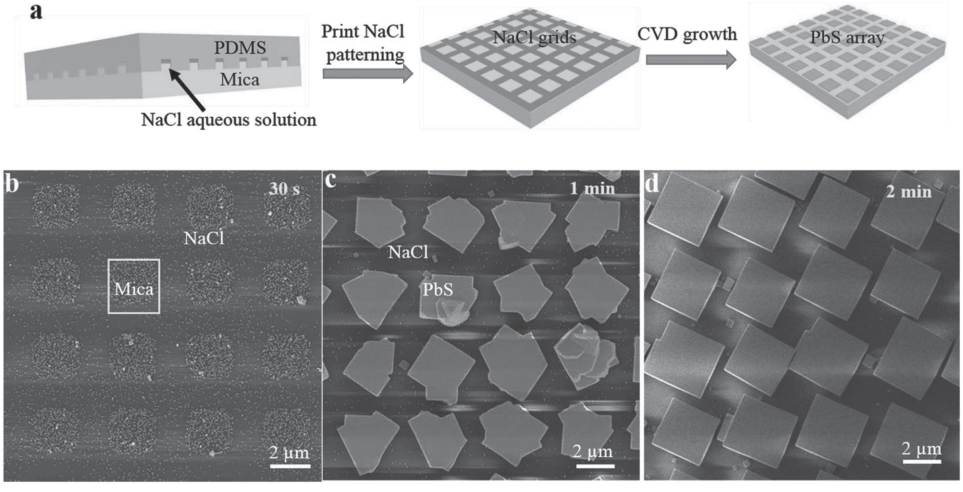


**Figure 4.** The growing mechanism of 2D PbS nanoplates arrays. a) Schematic representation of procedures for patterning of 2D PbS nanoplates arrays. The SEM images of the PbS nanoplates arrays under different reaction time b) 30 s, c) 1 min, d) 2 min.

1 min, plenty of irregular nanoplatelets can be observed and tend to coalesce with each other, as shown in Figure 4c and Figure S6 (Supporting Information). The driving force of the coalescence process is the reduction of edge energy through decreasing their total edge length.[20] Finally, when the reaction time extends to 2 min, regular square nanoplates appear with final exposed four equivalent {200} crystal surfaces. Remarkable, the growing mechanism in our case is different with previous reports about controlling the nucleation site.[42] As shown in Figure 4c,d, only very small PbS nanoplates can be find on NaCl-modified surface. It further demonstrates that the NaCl-modified surface of mica is highly rough, which hinders the vdWE of PbS.

In summary, by utilizing the nature of low surface energy of graphite, we successfully conducted the van der Waals epitaxial growth of ultrathin 2D PbS nanoplates with thickness of ranging from 5 to 35 nm. The PbS nanoplates are single crystalline with cubic symmetry and display superior infrared response with photoresponsivity, detectivity, switching time, and photogain values as high as 1621 A $W^{-1}$, $1.72 \times 10^{11}$ Jones, 0.3 s, and 2512 respectively. Further considering the epitaxial relation between layered mica and PbS and using NaCl to define the position of vdWE, we realize the orientation-controlled and well-defined single-crystalline square PbS nanopates arrays on mica. The edges of square nanoplates orient predominantly at multiples of 90°. The square PbS nanopates arrays are promising in the application of high-performance integrated optoelectronic devices.

## Experimental Section

*The Experimental Details about the Growth of PbS Nanoplates*: The graphite was peeled off with the tape by standard mechanically exploitation method. Then graphite was transferred to surface of $SiO_2$/Si substrate. Mica was first intaglio printed by NaCl aqueous solution using a polydimethylsiloxane (PDMS) stamp. Then, mica with NaCl aqueous solution (0.01 mol $L^{-1}$) was heated to 150 °C using a heating belt. Finally, the mica surface modified with periodic arrays was released from the PDMS stamp. The substrates and the PbS powder (99.999%, Alfa Aesar) were placed into CVD furnace. Before the experiments, the quartz tube was evacuated three times by the pump and flushed with argon. Then $H_2$ at a constant flow rate of 20 sccm was supplied to the tube. During the growth, the temperatures of the precursor and substrates were set to 750 °C and 500 °C, respectively. The reaction continued for 2 min. At last, the furnace naturally cooled to room temperature.

*Microstructure Characterization*: The morphology was characterized by optical microscopy (Leica DM4000M microscope), field emission scanning electron microscopy (Hitachi S4800), AFM (Dimension 3100). Then the crystal structure was analyzed by high-resolution transmission electron microscope (HRTEM) on FEI Tecnai F20 with selected area electron diffraction (SAED).

*Device Fabrication and Measurements*: PbS nanoplates were transferred onto clean $SiO_2$/Si substrate from mica by a flexible polydimethylsiloxane(PDMS) layer. The source and drain electrodes were written on PbS nanoplate by standard electron-beam lithography (EBL). Subsequently, 5 nm Cr and 100 nm Au were deposited on surface of PbS. The devices were measured in a manual probe station (Everbeing, BD4) with a sealed chamber. The parameters were analyzed using a Keithley 4200 semiconductor characterization system. All the measurements were carried out in a vacuum of $\approx 10^{-6}$ torr at room temperature. The source and drain electrodes of PbS arrays were prepared by FEI Nanolab 600i SEM/FIB dual-beam system.

## Supporting Information

Supporting Information is available from the Wiley Online Library or from the author.

## Acknowledgements

Y.W. and Q.W. contributed equally to the work. This work was supported by the National Natural Science Foundation of China (Nos. 21373065, 61474033, and 61574050), Strategic Priority Research Program of the Chinese Academy of Sciences (Grant No. XDA09040201), 973 Program of the Ministry of Science and Technology of China (No. 2012CB934103), and CAS Key Laboratory of Nanosystem and Hierarchical Fabrication. The authors also gratefully acknowledge the support of Youth Innovation Promotion Association CAS.

Received: May 10, 2016
Revised: June 2, 2016
Published online:

[1] K. S. Novoselov, A. K. Geim, S. V. Morozov, D. Jiang, Y. Zhang, S. V. Dubonos, I. V. Grigorieva, A. A. Firsov, *Science* **2004**, *306*, 666.
[2] S. Najmaei, Z. Liu, W. Zhou, X. Zou, G. Shi, S. Lei, B. I. Yakobson, J.-C. Idrobo, P. M. Ajayan, J. Lou, *Nat. Mater.* **2013**, *12*, 754.
[3] H. Li, J. Cao, W. Zheng, Y. Chen, D. Wu, W. Dang, K. Wang, H. Peng, Z. Liu, *J. Am. Chem. Soc.* **2012**, *134*, 6132.
[4] X. Wang, Y. Ouyang, X. Li, H. Wang, J. Guo, H. Dai, *Phys. Rev. Lett.* **2008**, *100*, 206803.
[5] a) K. S. Novoselov, A. K. Geim, S. V. Morozov, D. Jiang, M. I. Katsnelson, I. V. Grigorieva, S. V. Dubonos, A. A. Firsov, *Nature* **2005**, *438*, 197; b) Y. Zhang, Y.-W. Tan, H. L. Stormer, P. Kim, *Nature* **2005**, *438*, 201.
[6] K. Takada, H. Sakurai, E. Takayama-Muromachi, F. Izumi, R. A. Dilanian, T. Sasaki, *Nature* **2003**, *422*, 53.
[7] C.-Z. Chang, J. Zhang, X. Feng, J. Shen, Z. Zhang, M. Guo, K. Li, Y. Ou, P. Wei, L.-L. Wang, Z.-Q. Ji, Y. Feng, S. Ji, X. Chen, J. Jia, X. Dai, Z. Fang, S.-C. Zhang, K. He, Y. Wang, L. Lu, X.-C. Ma, Q.-K. Xue, *Science* **2013**, *340*, 167.
[8] A. A. Balandin, *Nat. Mater.* **2011**, *10*, 569.
[9] a) C. Zhu, Z. Zeng, H. Li, F. Li, C. Fan, H. Zhang, *J. Am. Chem. Soc.* **2013**, *135*, 5998; b) F. K. Perkins, A. L. Friedman, E. Cobas, P. M. Campbell, G. G. Jernigan, B. T. Jonker, *Nano Lett.* **2013**, *13*, 668.
[10] a) D. J. Late, B. Liu, J. Luo, A. Yan, H. S. S. R. Matte, M. Grayson, C. N. R. Rao, V. P. Dravid, *Adv. Mater.* **2012**, *24*, 3549; b) C. R. Dean, A. F. Young, I. Meric, C. Lee, L. Wang, S. Sorgenfrei, K. Watanabe, T. Taniguchi, P. Kim, K. L. Shepard, J. Hone, *Nat. Nano* **2010**, *5*, 722.
[11] L. Cheng, J. Liu, X. Gu, H. Gong, X. Shi, T. Liu, C. Wang, X. Wang, G. Liu, H. Xing, W. Bu, B. Sun, Z. Liu, *Adv. Mater.* **2014**, *26*, 1886.
[12] S. Lei, L. Ge, Z. Liu, S. Najmaei, G. Shi, G. You, J. Lou, R. Vajtai, P. M. Ajayan, *Nano Lett.* **2013**, *13*, 2777.
[13] X.-J. Wu, J. Chen, C. Tan, Y. Zhu, Y. Han, H. Zhang, *Nat. Chem.* **2016**, 8, 470.
[14] Y. Liu, X. Hua, C. Xiao, T. Zhou, P. Huang, Z. Guo, B. Pan, Y. Xie, *J. Am. Chem. Soc.* **2016**, 138, 5087.
[15] A. L. Briseno, S. C. B. Mannsfeld, M. M. Ling, S. Liu, R. J. Tseng, C. Reese, M. E. Roberts, Y. Yang, F. Wudl, Z. Bao, *Nature* **2006**, *444*, 913.
[16] Y. Zhou, Y. Nie, Y. Liu, K. Yan, J. Hong, C. Jin, Y. Zhou, J. Yin, Z. Liu, H. Peng, *ACS Nano* **2014**, *8*, 1485.

[17] Y. Guo, M. Aisijiang, K. Zhang, W. Jiang, Y. Chen, W. Zheng, Z. Song, J. Cao, Z. Liu, H. Peng, *Adv. Mater.* **2013**, *25*, 5959.
[18] W. Zheng, T. Xie, Y. Zhou, Y. L. Chen, W. Jiang, S. Zhao, J. Wu, Y. Jing, Y. Wu, G. Chen, Y. Guo, J. Yin, S. Huang, H. Q. Xu, Z. Liu, H. Peng, *Nat. Commun.* **2015**, *6*, 6972.
[19] G. Wang, D. Li, H.-C. Cheng, Y. Li, C.-Y. Chen, A. Yin, Z. Zhao, Z. Lin, H. Wu, Q. He, M. Ding, Y. Liu, Y. Huang, X. Duan, *Sci. Adv.* **2015**, *1*, 1500613.
[20] L. Niu, X. Liu, C. Cong, C. Wu, D. Wu, T. R. Chang, H. Wang, Q. Zeng, J. Zhou, X. Wang, W. Fu, P. Yu, Q. Fu, S. Najmaei, Z. Zhang, B. I. Yakobson, B. K. Tay, W. Zhou, H. T. Jeng, H. Lin, T. C. Sum, C. Jin, H. He, T. Yu, Z. Liu, *Adv. Mater.* **2015**, *27*, 7800.
[21] Q. Wang, M. Safdar, K. Xu, M. Mirza, Z. Wang, J. He, *ACS Nano* **2014**, *8*, 7497.
[22] Q. Wang, K. Xu, Z. Wang, F. Wang, Y. Huang, M. Safdar, X. Zhan, F. Wang, Z. Cheng, J. He, *Nano Lett.* **2015**, *15*, 1183.
[23] Q. Wang, Y. Wen, F. Yao, Y. Huang, Z. Wang, M. Li, X. Zhan, K. Xu, F. Wang, F. Wang, J. Li, K. Liu, C. Jiang, F. Liu, J. He, *Small* **2015**, *11*, 5388.
[24] G. Konstantatos, I. Howard, A. Fischer, S. Hoogland, J. Clifford, E. Klem, L. Levina, E. H. Sargent, *Nature* **2006**, *442*, 180.
[25] A. Rogalski, *Prog. Quantum Electron.* **2003**, *27*, 59.
[26] a) P. L. Nichols, Z. Liu, L. Yin, S. Turkdogan, F. Fan, C. Z. Ning, *Nano Lett.* **2015**, *15*, 909; b) E. M. Miller, D. M. Kroupa, J. Zhang, P. Schulz, A. R. Marshall, A. Kahn, S. Lany, J. M. Luther, M. C. Beard, C. L. Perkins, J. van de Lagemaat, *ACS Nano* **2016**, *10*, 3302.
[27] a) R. Schodel, T. Ott, R. Genzel, R. Hofmann, M. Lehnert, A. Eckart, N. Mouawad, T. Alexander, M. J. Reid, R. Lenzen, M. Hartung, F. Lacombe, D. Rouan, E. Gendron, G. Rousset, A. M. Lagrange, W. Brandner, N. Ageorges, C. Lidman, A. F. M. Moorwood, J. Spyromilio, N. Hubin, K. M. Menten, *Nature* **2002**, *419*, 694; b) S. Rawlings, M. Lacy, K. M. Blundell, S. A. Eales, A. J. Bunker, S. T. Garrington, *Nature* **1996**, *383*, 502; c) R. Ettl, I. Chao, F. Diederich, R. L. Whetten, *Nature* **1991**, *353*, 149.
[28] S. A. McDonald, G. Konstantatos, S. Zhang, P. W. Cyr, E. J. D. Klem, L. Levina, E. H. Sargent, *Nat. Mater.* **2005**, *4*, 138.
[29] X.-B. Li, P. Guo, Y.-N. Zhang, R.-F. Peng, H. Zhang, L.-M. Liu, *J. Mater. Chem. C* **2015**, *3*, 6284.
[30] M. Aerts, T. Bielewicz, C. Klinke, F. C. Grozema, A. J. Houtepen, J. M. Schins, L. D. A. Siebbeles, *Nat. Commun.* **2014**, *5*, 3789.
[31] G. Konstantatos, M. Badioli, L. Gaudreau, J. Osmond, M. Bernechea, F. P. G. de Arquer, F. Gatti, F. H. L. Koppens, *Nat. Nano* **2012**, *7*, 363.
[32] Z. Sun, Z. Liu, J. Li, G.-a. Tai, S.-P. Lau, F. Yan, *Adv. Mater.* **2012**, *24*, 5878.
[33] D. Kufer, I. Nikitskiy, T. Lasanta, G. Navickaite, F. H. L. Koppens, G. Konstantatos, *Adv. Mater.* **2015**, *27*, 176.
[34] W. Zheng, W. Feng, X. Zhang, X. Chen, G. Liu, Y. Qiu, T. Hasan, P. Tan, P. A. Hu, *Adv. Funct. Mater.* **2016**, 26, 2648.
[35] J. Schornbaum, B. Winter, S. P. Schießl, F. Gannott, G. Katsukis, D. M. Guldi, E. Spiecker, J. Zaumseil, *Adv. Funct. Mater.* **2014**, *24*, 5798.
[36] H. Heo, J. H. Sung, G. Jin, J.-H. Ahn, K. Kim, M.-J. Lee, S. Cha, H. Choi, M.-H. Jo, *Adv. Mater.* **2015**, *27*, 3803.
[37] Y. Hernandez, V. Nicolosi, M. Lotya, F. M. Blighe, Z. Sun, S. De, I. T. McGovern, B. Holland, M. Byrne, Y. K. Gun'Ko, J. J. Boland, P. Niraj, G. Duesberg, S. Krishnamurthy, R. Goodhue, J. Hutchison, V. Scardaci, A. C. Ferrari, J. N. Coleman, *Nat. Nano* **2008**, *3*, 563.
[38] Z. Wang, K. Xu, Y. Li, X. Zhan, M. Safdar, Q. Wang, F. Wang, J. He, *ACS Nano* **2014**, *8*, 4859.
[39] F. Wang, Z. Wang, K. Xu, F. Wang, Q. Wang, Y. Huang, L. Yin, J. He, *Nano Lett.* **2015**, *15*, 7558.
[40] Q. Wang, J. Li, Y. Lei, Y. Wen, Z. Wang, X. Zhan, F. Wang, F. Wang, Y. Huang, K. Xu, J. He, *Adv. Mater.* **2016**, 28, 3596.
[41] Y. Guo, Z. Liu, H. Peng, *Small* **2015**, *11*, 3290.
[42] a) G. H. Han, N. J. Kybert, C. H. Naylor, B. S. Lee, J. Ping, J. H. Park, J. Kang, S. Y. Lee, Y. H. Lee, R. Agarwal, A. T. C. Johnson, *Nat. Commun.* **2015**, *6*, 6128; b) Q. Yu, L. A. Jauregui, W. Wu, R. Colby, J. Tian, Z. Su, H. Cao, Z. Liu, D. Pandey, D. Wei, T. F. Chung, P. Peng, N. P. Guisinger, E. A. Stach, J. Bao, S.-S. Pei, Y. P. Chen, *Nat. Mater.* **2011**, *10*, 443; c) G. Su, V. G. Hadjiev, P. E. Loya, J. Zhang, S. Lei, S. Maharjan, P. Dong, P. M. Ajayan, J. Lou, H. Peng, *Nano Lett.* **2015**, *15*, 506.